Atmos. Meas. Tech. Discuss., 8, 811–855, 2015
www.atmos-meas-tech-discuss.net/8/811/2015/
doi:10.5194/amtd-8-811-2015

Atmospheric Measurement Techniques Discussions
Open Access

Dynamic statistical optimization of GNSS radio occultation bending angles: an advanced algorithm and its performance analysis

Y. Li[1,2], G. Kirchengast[3,2], B. Scherllin-Pirscher[3], R. Norman[2], Y. B. Yuan[1], J. Fritzer[3], M. Schwaerz[3], and K. Zhang[2]

[1]State Key Laboratory of Geodesy and Earth's Dynamics, Institute of Geodesy and Geophysics (IGG), Chinese Academy of Sciences, Wuhan, China
[2]Satellite Positioning for Atmosphere, Climate, and Environment (SPACE) Research Centre, RMIT University, Melbourne, Victoria, Australia
[3]Wegener Center for Climate and Global Change (WEGC) and Institute for Geophysics, Astrophysics, and Meteorology/Institute of Physics (IGAM/IP), University of Graz, Graz, Austria

Received: 1 November 2014 – Accepted: 16 December 2014 – Published: 22 January 2015

Correspondence to: Y. Li (lovewud123.ying.li@gmail.com)

Published by Copernicus Publications on behalf of the European Geosciences Union.

Dynamic statistical optimization of GNSS radio occultation bending angles
Y. Li et al.

Abstract

We introduce a new dynamic statistical optimization algorithm to initialize ionosphere-corrected bending angles of Global Navigation Satellite System (GNSS) based radio occultation (RO) measurements. The new algorithm estimates background and observation error covariance matrices with geographically-varying uncertainty profiles and realistic global-mean correlation matrices. The error covariance matrices estimated by the new approach are more accurate and realistic than in simplified existing approaches and can therefore be used in statistical optimization to provide optimal bending angle profiles for high-altitude initialization of the subsequent Abel transform retrieval of refractivity. The new algorithm is evaluated against the existing Wegener Center Occultation Processing System version 5.6 (OPSv5.6) algorithm, using simulated data on two test days from January and July 2008 and real observed CHAMP and COSMIC measurements from the complete months of January and July 2008. The following is achieved for the new method's performance compared to OPSv5.6: (1) significant reduction in random errors (standard deviations) of optimized bending angles down to about two-thirds of their size or more; (2) reduction of the systematic differences in optimized bending angles for simulated MetOp data; (3) improved retrieval of refractivity and temperature profiles; (4) produces realistically estimated global-mean correlation matrices and realistic uncertainty fields for the background and observations. Overall the results indicate high suitability for employing the new dynamic approach in the processing of long-term RO data into a reference climate record, leading to well characterized and high-quality atmospheric profiles over the entire stratosphere.

1 Introduction

Global Navigation Satellite System (GNSS) based radio occultation (RO) is a robust atmospheric remote sensing technique that provides accurate atmospheric profiles of the Earth's atmosphere (Kursinski et al., 1997; Hajj et al., 2002; Kirchengast, 2004). This

AMTD
8, 811–855, 2015

technique has several distinctive advantages in terms of high accuracy, high vertical resolution, global coverage, and self-calibration (Anthes, 2011; Yu et al., 2014). GNSS RO data are now widely used in numerical weather prediction, climate monitoring, and space weather research (e.g., Healy and Eyre, 2000; Cucurull and Derber, 2008; Le Marshall et al., 2010; Anthes, 2011; Steiner et al., 2011; Carter et al., 2013).

Although the RO technique has now been rather successful, it still suffers from some weaknesses. For example, the RO observations are affected by higher-order ionospheric effects and observation errors at high altitudes (> 30 km) (Bassiri and Hajj, 1993; Danzer et al., 2013; Liu et al., 2013). These errors propagate downward from bending angles to refractivity through the Abel integral and also degrade the accuracy of the retrieved temperature and other atmospheric profiles (Healy, 2001; Rieder and Kirchengast, 2001; Gobiet and Kirchengast, 2004; Steiner and Kirchengast, 2005). Therefore, it is very important to have a best-possible initialization of the ionosphere-corrected bending angles at high altitudes for more accurate climate monitoring.

Statistical optimization is a commonly used method to initialize RO bending angles at high altitudes (e.g., Sokolovskiy and Hunt, 1996; Gorbunov et al., 1996; Hocke, 1997; Healy, 2001; Gorbunov, 2002; Gobiet and Kirchengast, 2004; Gobiet et al., 2007). It is a generalized least squares approach that combines an observed RO bending angle profile with a background bending angle profile (Turchin and Nozik, 1969; Rodgers, 1976, 2000). The weights of the two types of bending angles are determined by the inverse of their error covariance matrices. The statistical optimization equation used is (Healy, 2001; Gobiet and Kirchengast, 2004):

$$\alpha_{\mathrm{SO}} = \alpha_{\mathrm{b}} + \mathbf{C}_{\mathrm{b}}(\mathbf{C}_{\mathrm{b}} + \mathbf{C}_{\mathrm{o}})^{-1} \cdot (\alpha_{\mathrm{o}} - \alpha_{\mathrm{b}}), \quad (1)$$

where α_{SO} is the statistically optimized bending angle, α_{b} and α_{o} are the respective (unbiased) background and observed bending angle profiles, and $\mathbf{C}_{\mathrm{b}}$ and $\mathbf{C}_{\mathrm{o}}$ are the corresponding error covariance matrices.

In statistical optimization, the more accurately the error covariance matrices represent the error characteristics the more accurate is the optimized bending angle profile.

However, it is not straightforward to obtain such suitable error covariance matrices, especially for the background bending angle errors since they are neither supplied together with common climatological models nor is the construction a straightforward task. Therefore, previous approaches usually simplified the calculation of the error covariance matrices.

A typical approach is to estimate the background error covariance matrix by assuming a constant relative standard error of the background bending angle and a simple error correlation structure like exponential fall-off over an atmospheric scale height (Healy, 2001; Rieder and Kirchengast, 2001; Gobiet and Kirchengast, 2004) or disregarding correlations (Sokolovskiy and Hunt, 1996; Gorbunov et al., 1996, 2005, 2006; Hocke, 1997; Gorbunov, 2002; Lohmann, 2005). Similarly, the observation error covariance matrix is formulated from estimating the observation error at a defined mesospheric altitude range (where the RO signal is weak) and using simple exponential fall-off error correlations (Healy, 2001; Gobiet and Kirchengast, 2004) or again just ignoring the latter. These rough estimations generally result in inaccurate error covariance matrices and therefore result in inaccurate optimized bending angles that degrade the accuracy of subsequently retrieved atmospheric profiles. More details on the various schemes are provided by a review recently of existing algorithms given by Li et al. (2013), Sect. 2.1 therein.

Improved accuracy in optimized bending angles was obtained when using an improved statistical optimization algorithm to initialize ionosphere-corrected bending angles (Li, 2013; Li et al., 2013). Li et al. (2013) used European Centre for Medium-Range Weather Forecasts (ECMWF) short-range (24 h) forecast fields as background bending angles. Their background error covariance matrix was accurately and realistically estimated using large ensembles of ECMWF short-range forecast, analysis, and RO observed bending angles. It was constructed using daily global fields of estimated background uncertainty profiles and a daily global-mean correlation matrix. The background uncertainty profile was dynamically estimated taking into account its variations with latitude, longitude, altitude, and day of year. They did not only calculate the ran-

AMTD
8, 811–855, 2015

dom errors of background bending angles using large ensembles of ECMWF and RO data, but also empirically modeled the potential systematic background uncertainty and finally combined these two uncertainties to formulate the background uncertainty. The global-mean correlation matrix was also calculated using large ensembles of ECMWF analysis and forecast fields. Finally, the biases in the background bending angle were corrected to avoid the potential effects on the optimized bending angles from the biases.

Since this first-version dynamic statistical optimization algorithm dynamically estimated the background error covariance matrix only, it is hereafter referred to as the b-dynamic algorithm ("b" represents background) in this study. The b-dynamic algorithm was evaluated by Li et al. (2013) against the Occultation Processing System version 5.4 (OPSv5.4) algorithm developed by the Wegener Center for Climate and Global Change (WEGC) (Pirscher, 2010; Ho et al., 2012; Steiner et al., 2013). It was found that the b-dynamic algorithm significantly reduced random errors of the optimized bending angles and left less or about equal levels of residual systematic errors. The quality of the subsequently retrieved refractivity and temperature profiles was also improved. In addition, the dynamically estimated background error correlation matrix alone was able to already improve the optimized bending angles.

The aim of this study is to obtain even more accurate and reliable atmospheric profiles for optimal climate monitoring by advancing the b-dynamic algorithm to a complete dynamical estimation of both background and observation uncertainties and correlations. This is accomplished by employing a realistically estimated observation error covariance matrix in addition to the b-dynamic formulation. The observation error covariance matrix is constructed with dynamically estimated observation uncertainties for each occultation event and daily global-mean correlation matrices from large ensembles of data. The observation uncertainty is calculated using bias-corrected difference profiles of observed RO bending angle profiles relative to corresponding co-located ECMWF forecast bending angle profiles. The global-mean correlation matrix is calculated using multiple days of RO bending angle profiles and corresponding co-located

AMTD
8, 811–855, 2015

ECMWF analysis bending angle profiles. In addition, the basic b-dynamic algorithm is also updated as part of the dynamic algorithm for obtaining even more robust background error covariance matrices. Finally, the stability of the new dynamic algorithm is evaluated using full months of RO data from CHAMP and COSMIC while Li et al. (2013) used a couple of individual days for initial evaluation of the b-dynamic algorithm.

The structure of this paper is as follows. Section 2 introduces the methodology of the dynamic statistical optimization algorithm. Section 3 evaluates its performance using both simulated and observed RO data. Finally a summary and conclusions are given in Sect. 4.

2 The new dynamic statistical optimization algorithm

Figure 1 shows the algorithmic steps of the dynamic statistical optimization algorithm. The new algorithm mainly includes two parts: (1) the dynamic estimation of the background error covariance matrix and the bias-correction of background bending angles; and (2) the dynamic estimation of the observation error covariance matrix. Information on background/observation uncertainty and on the background/observation correlation matrix is needed for constructing complete background/observation error covariance matrices. The uncertainty at any given vertical level is the square root of the diagonal value of the error covariance matrix at that level. The correlation matrix includes correlation functions for each vertical level, which comprise all correlation coefficients of an error at a given vertical level to the errors at other levels. In summary, the background/observation uncertainties and the corresponding correlation matrix together formulate the background/observation error covariance matrices (Gaspari and Cohn, 1999).

Assuming $k = 1, \ldots, N_{\mathrm{occ}}$ being sequentially numbered RO events of a day, then for each occultation event k the dynamic algorithm estimates the (unbiased) background bending angle profile α_{b}^{k} and its corresponding error covariance matrix $\mathbf{C}_{\mathrm{b}}^{k}$, as well as the observation error covariance matrix $\mathbf{C}_{\mathrm{o}}^{k}$. Using these three quantities together with

AMTD
8, 811–855, 2015

the observed bending angle α_o^k, the statistically optimized bending angle profile α_{SO}^k can be determined as

$$\alpha_{SO}^k = \alpha_b^k + \mathbf{C}_b^k \left(\mathbf{C}_b^k + \mathbf{C}_o^k\right)^{-1} \cdot \left(\alpha_o^k - \alpha_b^k\right). \tag{2}$$

The algorithm for the estimation of α_b^k and $\mathbf{C}_b^k$ has been described in detail by Li et al. (2013) as part of introducing the b-dynamic algorithm. It will be briefly described in Sect. 2.1, focusing on recalling the key algorithmic steps and the advances in the dynamic algorithm. In Sect. 2.2, details on how to estimate $\mathbf{C}_o^k$ and other issues that are critical to the capability of the dynamic algorithm are provided.

2.1 Dynamic estimation of the background error covariance matrix and bias-calibration of background bending angles

The dynamic estimation of the background error covariance matrix includes three algorithmic steps, (1) construction of basic daily background fields (blue boxes in the left part of Fig. 1, (2) preparation of the derived daily background fields (green boxes), and (3) dynamic estimation of the background error covariance matrix (orange boxes).

In the first step, daily fields of the basic background variables are prepared for statistical optimization using 10° latitude × 20° longitude grids (centered at the base cell at 5° N, 10° E), at 400 levels from 0.2 to 80.0 km with 200 m steps. This construction of background variables allows us to suitably capture large-scale background error dynamics as a function of latitude, longitude, (impact) altitude, and time, and yields daily fields using a global 18 × 18 × 400 grid. The basic statistical mean variables as shown in step 1 of Fig. 1 are calculated on this 18 × 18 × 400 grid and saved into daily data files. Compared to the b-dynamic algorithm, which used 200 representative impact altitude levels from 0.1 to 80.0 km with non-equidistant spacing, this new scheme allows direct use of these variables for the next step of calculation, avoiding additional interpolation of all variables and particularly also within correlation matrices.

AMTD
8, 811–855, 2015

The data used to calculate these basic background variables include ECMWF analysis fields and corresponding 24 h forecast fields with a T42L91 resolution at 00:00 and 12:00 UTC, and observed bending angles. In calculating the mean variables in each grid cell, time-averaging over seven days (from three days before to three days after the day of interest) and horizontal-averaging over geographic domains of at least 1000 km × 3000 km (over 10° latitude × 60° longitude cells from 60° S to 60° N latitude, poleward over larger longitude ranges of 95° from 60 to 70° N/S, 120° from 70 to 80° N/S, and 270° from 80 to 90° N/S) were used. Compared to the b-dynamic scheme, which used 5 days of data only and smaller geographic regions (1000 km × 1000 km) for averaging, this update allows more data to be used for a more reliable statistical estimation (especially for mean observed bending angles) at each 10° latitude × 20° longitude grid point. The calculation of these basic mean variables includes mean variables, the construction of error correlation matrices, and empirical modeling. For details on the estimation of these basic variables refer to Li et al. (2013).

The second step involves the preparation of the derived daily background fields. These specific statistical quantities include: (i) the forecast-minus-analysis standard deviations $s_{\mathrm{f-a}}$, which represent the estimated random uncertainty of the background bending angles, (ii) the estimated uncertainty of the mean background bending angle u_{b}, and (iii) the difference between the mean forecast bending angle and the mean background bending angle $\Delta\overline{\alpha}_{\mathrm{f-b}}$.

In the third step, the background error covariance matrix is calculated using the variables on from the fields obtained in step 2. Co-located profiles of $\Delta\overline{\alpha}^{k}_{\mathrm{f-b}}$, u^{k}_{b}, and $s^{k}_{\mathrm{f-a}}$ are derived by bi-linear interpolation to the RO event location. The combined background standard uncertainty profile $u^{\mathrm{occ}}_{\mathrm{b}}$ is then calculated as

$$u^{\mathrm{occ}}_{\mathrm{b}} = \left[\left(f_{\mathrm{bcvg}} \cdot u^{k}_{\mathrm{b}}\right)^{2} + \left(s^{k}_{\mathrm{f-a}}\right)^{2}\right]^{1/2}. \tag{3}$$

Herein the bias coverage factor f_{bcvg} is employed to strongly penalize the estimated bias-type uncertainty u^{k}_{b} relative to the estimated random uncertainty $s^{k}_{\mathrm{f-a}}$. This mini-

AMTD
8, 811–855, 2015

Dynamic statistical optimization of GNSS radio occultation bending angles

Y. Li et al.

mizes the influence from potential residual background biases, relative to observation uncertainty, on the resulting optimized profile α^k_{SO}. In this study $f_{\mathrm{bcvg}} = 5$ was used, consistent with Li et al. (2013), while in future long-term application for climate processing this may be further tuned to enable altitude-dependency and an even stronger background penalty within the stratosphere.

Using the background standard uncertainty and the global-mean correlation matrix $\mathbf{R}_{\mathrm{f-a}} = R_{\mathrm{f-a},ij}$, the background error covariance matrix $\mathbf{C}^k_{\mathrm{b}} = C^k_{\mathrm{b},ij}$ is formulated as

$$C^k_{\mathrm{b},ij} = u^{\mathrm{occ}}_{\mathrm{b},i} \cdot u^{\mathrm{occ}}_{\mathrm{b},j} \cdot R_{\mathrm{f-a},ij}. \quad (4)$$

Furthermore, in order to effectively reduce the residual bias in the background bending angle α^k_{b} (cf. Eq. 2) to within the estimated uncertainty of the background mean u^k_{b}, α^k_{b} is calculated by subtracting the forecast-minus-background mean difference $\Delta\overline{\alpha}^k_{\mathrm{f-b}}$ from the co-located forecast bending angle α^k_{f},

$$\alpha^k_{\mathrm{b}} = \alpha^k_{\mathrm{f}} - \Delta\overline{\alpha}^k_{\mathrm{f-b}}. \quad (5)$$

Figure 2 illustrates zonal-mean fields of the relative uncertainty of forecast-minus-analysis standard deviations $100 \cdot \left(s_{\mathrm{f-a}}/\overline{\alpha}_{\mathrm{a}}\right)$ (top) and of the relative uncertainty of estimated (and penalized) residual background biases $100 \cdot \left(f_{\mathrm{bcvg}} \cdot u_{\mathrm{b}}\right)/\alpha_{\mathrm{a}}$ (bottom), respectively, where $\overline{\alpha}_{\mathrm{a}}$ is the ECMWF analysis mean bending angle. As a function of latitude (left), forecast-minus-analysis standard deviation reveals largest errors at high altitudes over the Antarctic region. The relative standard deviations are larger than 10 % near 80 km, decreasing to ∼ 5 % at 70 km and to ∼ 3 % at 50 km and remain at ∼ 1 % below 25 km. In non-polar regions, the standard deviations amount approximately to 3 to 4 % near 80 km, decrease to 2 % at 75 km and remain within 1 to 2 % below. The day-to-day temporal evolution of $s_{\mathrm{f-a}}$ at high southern latitudes (60 to 70° S) (right) reveals relatively smooth uncertainty conditions for the entire July, without much temporal dynamics in the uncertainty. In course of testing, it was found that the estimates are

AMTD
8, 811–855, 2015

consistent with flow-dependent forecast-minus-analysis error estimates produced by ECMWF's ensemble of data assimilations (EDA) system (Isaksen et al., 2010; Bonavita et al., 2011; M. Bonavita, ECMWF, personal communication, 2012).

Regarding variations of $100 \cdot \left(f_{\text{bcvg}} \cdot u_{\text{b}}^{k}\right) / \overline{\alpha}_{\text{a}}^{k}$ as a function of latitude (bottom left), the bias-type uncertainties are also largest at high altitudes in the Southern Hemisphere. The relative uncertainties are larger than 35 % near 80 km, decreasing to 25 % at 60 km and remain smaller than 5 % below 40 km. In non-polar regions, the relative uncertainties amount to 20 % near 80 km, decreasing to 5 % also at 40 km. The temporal evolution of the systematic uncertainty $100 \cdot \left(f_{\text{bcvg}} \cdot u_{\text{b}}^{k}\right) / \overline{\alpha}_{\text{a}}^{k}$ over a month (bottom right) shows that also these relative uncertainties reveal little sub-monthly variations, due to the way of construction (Li et al., 2013).

Figure 3 shows exemplary global mean correlation functions (left) and associated correlation lengths estimated from these functions (right) for the days of 5, 15, and 25 July 2008. The correlation functions with peaks at three representative height levels (30, 50, 70 km) are evidently rather similar over the month. Their main property is that the main peaks of the functions are close to Gaussian shape and from the main peak outwards there are negative side peaks at each side. Further outward, small secondary positive peaks occur after which the functions then essentially approach zero. Regarding the correlation lengths, it increases rather smoothly with altitude from about 0.8 km at 20 km to near 6 km at 80 km and also shows little variation over the example month of July 2008.

Overall this behavior indicates that in months without larger atmospheric anomalies (such as for example sudden stratospheric warming at high latitudes; Klingler, 2014), a daily update of correlation matrices is not necessarily needed. In a long-term application, however, it is never clear when and where some (transient) anomalies may occur so that daily update of the background fields was selected as a cautious baseline.

AMTD
8, 811–855, 2015
Dynamic statistical optimization of GNSS radio occultation bending angles
Y. Li et al.

2.2 Dynamic estimation of the observation error covariance matrix

The error covariance matrix of the observed bending angle C_{o}^{k} is calculated using an estimated observation uncertainty profile $u_{\mathrm{o}}^{\mathrm{occ}}$, estimated on a per-event basis, and a global-mean error correlation matrix $\mathbf{R}_{\mathrm{o}}^{\mathrm{occ}}$,

$$C_{\mathrm{o}}^{k} = u_{\mathrm{o},i}^{\mathrm{occ}} u_{\mathrm{o},j}^{\mathrm{occ}} R_{\mathrm{o},ij}^{\mathrm{occ}}. \quad (6)$$

Different to the OPSv5.6 and the b-dynamic algorithm, which estimate the observation uncertainty $u_{\mathrm{o}}^{\mathrm{occ}}$ between about 65 to 80 km with an MSIS bending angle profile as reference and assume the resulting value constant with altitude (Li et al., 2013), the full dynamic algorithm estimates $u_{\mathrm{o}}^{\mathrm{occ}}$ as a vertical profile over the stratopause region and mesosphere, using the co-located ECMWF forecast bending angle profile as reference.

More specifically, the first step is to subtract the co-located forecast bending angle profile α_{f}^{k} from the observed bending angle profile α_{o}^{k},

$$\Delta\alpha_{\mathrm{o}}^{k} = \alpha_{\mathrm{o}}^{k} - \alpha_{\mathrm{f}}^{k}. \quad (7)$$

The difference profile $\Delta\alpha_{\mathrm{o}}^{k}$ is then smoothed with a 15 km-window-width moving average (from 45 km to the top bound of the profile, usually 80 km). The resulting smoothed difference profile is denoted as $\overline{\Delta\alpha}_{\mathrm{o}}^{k}$.

The next step is to subtract the smoothed difference profile $\overline{\Delta\alpha}_{\mathrm{o}}^{k}$ from the original difference profile $\Delta\alpha_{\mathrm{o}}^{k}$ in order to obtain a delta-difference profile $\Delta\Delta\alpha_{\mathrm{o}}^{k}$ that essentially contains only random errors,

$$\Delta\Delta\alpha_{\mathrm{o}}^{k} = \Delta\alpha_{\mathrm{o}}^{k} - \overline{\Delta\alpha}_{\mathrm{o}}^{k}. \quad (8)$$

AMTD
8, 811–855, 2015

Finally the observation uncertainty at any impact altitude level i of each occultation event k, $u^k_{\mathrm{o},i}$, is calculated based on a moving window of 15 km width as

$$u^k_{\mathrm{o},i} = \sqrt{\frac{1}{n-1}\sum_{n=i_{z-7.5}}^{i_{z+7.5}}\left[\Delta\Delta\alpha^k_{\mathrm{o},n}\right]^2}, \tag{9}$$

where n is the number of sample points between $z_i + 7.5$ km and $z_i - 7.5$ km and where $i_{z-7.5}$ and $i_{z+7.5}$ denote the corresponding impact altitude indices. Equation (9) is only applied from 45 km to the top of the profile, providing $u^k_{\mathrm{o},i}$ estimates from 52.5 to 72.5 km; below/above the value at 52.5/72.5 km is extended downward/upward just as a constant value. The whole resulting profile then constitutes the observation uncertainty profile $u^{\mathrm{occ}}_{\mathrm{o}}$. This construction ensures that variations over the mesosphere can be accounted for while data below the stratopause, where the estimated delta-difference profile $\Delta\Delta\alpha^k_{\mathrm{o}}$ may also contain atmospheric variability noise (e.g., from gravity wave activity), are not allowed to influence the estimate.

Figure 4 illustrates the observation uncertainty profile $u^{\mathrm{occ}}_{\mathrm{o}}$, and intermediate variables from Eqs. (7) and (8), for six example RO events from 15 July 2008. The simMetOp events are simulated using the EGOPSv5.6 software in the same way as the simMetOp ensemble was produced by Li et al. (2013); for more details see Sect. 3 below. In each panel, the red line shows the original difference profile $\Delta\alpha^k_{\mathrm{o}}$ ("delta"), the blue line the smoothed difference profile $\overline{\Delta\alpha}^k_{\mathrm{o}}$ ("deltasmooth"), the green line the delta-difference profile $\Delta\Delta\alpha^k_{\mathrm{o}}$ ("deltadelta"), and the magenta line the observation uncertainty $u^{\mathrm{occ}}_{\mathrm{o}}$ ("Uncert"). It can be seen that Eqs. (7) and (8) are robust in removing systematic errors, leaving a good random signal, from which the uncertainty $u^{\mathrm{occ}}_{\mathrm{o}}$ is reliably estimated.

Estimated uncertainties are smallest (near 0.5 µrad) for the simMetOp events (top) that mimick MetOp/GRAS-type high performance receiver errors without additional noise effects (Li et al., 2013) and are distinctively larger for real data from CHAMP (middle) and COSMIC (bottom). The uncertainties of CHAMP and COSMIC bending angles can be quite variable, as illustrated, and can reach 10 µrad or more for CHAMP events while it is typically only around 2 µrad or so for COSMIC. Figure 4 also shows that the variation of uncertainty, which often may come from variations in ionospheric small-scale noise adding onto the RO receiver-related noise, can be well captured over the mesosphere.

The global-mean observation error correlation matrix $\mathbf{R}_o^{occ}$ is estimated using the difference profiles between the observed bending angle profiles and co-located ECMWF analysis bending angle profiles. In this estimation, we first construct a global-mean error covariance matrix using all available difference profiles from three days before to three days after the day of interest, i.e., using the same weekly smoother as for the background estimations. Then we derive the global mean correlation matrix by dividing all elements of the covariance matrix by its corresponding square-roots of diagonal values. RO observations used for this calculation included data from COSMIC and GRACE for January and July 2008, and MetOp-A data for July 2008 (no processed data were available for January 2008). The obtained correlation matrix $\mathbf{R}_o^{occ}$ is used based on Eq. (6) for the construction of observation error covariance matrices for all RO events of the day. For the convenience of use, it is also saved into the daily background and uncertainty fields data file so that the dynamic statistical optimization process can easily read in the data and use them for the event-by-event processing.

Figure 5 illustrates representative observation error correlation functions (extracted from $\mathbf{R}_o^{occ}$) and associated correlation lengths in the identical format as shown in Fig. 3 for the background error correlations, for ease of inter-comparison of the different characteristics. Comparing Figs. 3 and 5 it can be seen that the observation error correlation functions are basically similar in shape to the background error correlation functions (main peak, negative side peaks, smaller positive secondary side peaks) but with significantly shorter correlation lengths. In addition, the functional shape of side peaks is not as smooth as the one for the background. The correlation length is essentially constant at all altitudes of interest for the statistical optimization (above 30 km),

AMTD
8, 811–855, 2015

amounting to about 0.8 km. The intra-monthly variation is essentially negligible within the given July 2008 test month (applies also to January 2008, not shown), pointing to room for further improvement of the utility of the estimation for long-term processing, e.g., considering larger ensemble sizes and sub-global regions.

2.3 Other improvements of the new algorithm

In the b-dynamic algorithm of Li et al. (2013), the statistical optimization was applied exactly down to 30 km. However, for some noisy RO events especially from CHAMP, ionosphere-corrected bending angles can be still noisy at 30 km impact altitude. For these noisy events there can be a sharp change of bending angles characteristics from the rather smooth statistically-optimized data above 30 km to the rather noisy pure-observed data below 30 km. We have improved the algorithm in this respect as follows.

First, we gracefully adjust the observation uncertainty computed according to Sect. 2.2 for events which are still noisy near 30 km: if the estimated observation-to-background uncertainty (r_{OBU}) ratio is still larger than 0.2 at 30 km, we modify the r_{OBU} profile to make it linearly transit from the r_{OBU} value prevailing at 40 km to $r_{OBU} = 0.1$ at 28 km. Using this modified r_{OBU} profile, the observation uncertainty is then reconstructed below 40 km as $u_o(z_i) = r_{OBU}(z_i) \cdot u_b(z_i)$, enforcing increasing dominance of the observation information in the optimized profile towards 28 km.

Second, we apply the statistical optimization down to 28 km and then apply a half-sine weighted transition across 32 to 28 km between the statistically optimized bending angles and pure-observed bending angles. That is, the weighting function over this transition altitude range, $w(z_i)$, is estimated as

$$w(z_i) = 0.5 \cdot \left(\sin\left(\frac{\pi}{2} \cdot \frac{z_i - z_{SOoT}}{\Delta z_{SOoT}} \right) + 1 \right), \tag{10}$$

where z_{SOoT} is the statistically optimized-to-observed bending angle transition altitude, set to 30 km, and Δz_{SOoT} is the statistically optimized-to-observed bending angle tran-

AMTD
8, 811–855, 2015

sition half-width, set to 2 km. Employing $w(z_i)$ over the 32 km-to-28 km transition range in the form

$$\alpha_{\mathrm{SOoT}}(z_i) = w(z_i) \cdot \alpha_{\mathrm{SO}}(z_i) + (1 - w(z_i)) \cdot \alpha_{\mathrm{o}} \tag{11}$$

we get a well defined gradual transit from the optimized bending angles to observed bending angle. Applying these two improvements to the b-dynamic algorithm, the sometimes "spiky" behavior of some (CHAMP) profiles near the bottom boundary of statistical optimization discussed by Li et al. (2013) disappeared.

Another issue needing caution is the robustness of matrix inversions, especially related to the weighting matrix in Eq. (2), $\mathbf{C}_{\mathrm{b}}(\mathbf{C}_{\mathrm{b}} + \mathbf{C}_{\mathrm{o}})^{-1}$, containing the inversion of the summary matrix of the observation and background error covariance matrices. Since the observation error correlation functions can be insufficiently smooth and since the main peaks are close to Gaussian shape, the summary matrix can become close to ill-conditioned and cannot be accurately inverted in this case, inducing undue noise into the resulting weighting matrix.

This could be overcome by replacing the main peak by a 5th order polynomial function as described by Gaspari and Cohn (1999), which approximates a Gaussian shape and was also successfully used in the context of matrix inversion by Steiner and Kirchengast (2005), Eq. (5) therein (note that a typo leaked into the z^2 term as cited in this equation for $z < 1$; the correct denominator is "3" instead of "2", as in the z^2 term cited for $1 < z$ branch). After using this approximation, the inversion was sufficiently robust. Alternatives for ensuring robustness include the use of even larger ensemble sizes in matrix construction and more specialized methods of matrix inversion such as truncated singular-value-decomposition.

3 Evaluation of the new dynamic statistical optimization algorithm

The dynamic algorithm was implemented in the End-to-End GNSS Occultation Performance Simulation and Processing System (EGOPS) software version v5.6 (Fritzer et al., 2013) to enable a complete RO retrieval. The EGOPSv5.6 system was also used for all the simulation of RO observations (simMetOp events) and the retrieval of atmospheric profiles in this study. The standard RO data processing chain within this system is the OPSv5.6 retrieval.

We evaluated the new dynamic algorithm against this OPSv5.6 algorithm, which is, in terms of statistical optimization formulation, still the same as the OPSv5.4 algorithm used for comparison by Li et al. (2013). Briefly, the OPSv5.6 algorithm uses ECMWF short-range forecast bending angles as background and employs exponential fall-off functions to express the correlations of both background and observation uncertainties. The background uncertainty is modeled as amounting to 15 % of background bending angles. The observation uncertainty is estimated as the standard deviation of observed bending angles relative to co-located MSIS model bending angles in the impact altitude range from 65 to about 80 km. For more detailed information on OPSv5.6/v5.4 see Pirscher (2010), Steiner et al. (2013), and Schwaerz et al. (2013).

In addition to OPSv5.6 inter-comparison, the atmospheric profiles retrieved by the dynamic algorithm are compared with those retrieved by the b-dynamic algorithm (Li et al., 2013) and with those by the UCAR/COSMIC Data Analysis and Archive Center (CDAAC) Boulder.

The data sets used for the evaluation include simulated MetOp data (simMetOp) as well as real observed CHAMP and COSMIC data. simMetOp data were simulated in the same way as by Li et al. (2013), using moderate ionosphere condition using the NeUoG ionosphere model (Leitinger et al., 1996) in the forward simulations and using observational errors representing MetOp/GRAS-type receiving system errors.

As basis for the CHAMP and COSMIC retrievals, excess phase and orbit data were downloaded from UCAR/CDAAC Boulder (CDAAC data version 2009.2650 for CHAMP and 2010.2640 for COSMIC). CDAAC atmospheric profiles (atmPrf) used for the comparison of retrieved profiles are mainly from the same CDAAC data version. Recently reprocessed atmospheric profiles provided by CDAAC (version 2014.0140) are also used for comparison but due to very recent release only CHAMP was used so far.

We denote the CHAMP data version 2009.2650 as "CDAAC" in figure legends, and version 2014.0140 as "$CDAAC_{new}$". In the evaluation, retrieved RO profiles are shown relative to co-located reference profiles. For the CHAMP and COSMIC data, these co-located reference profiles were extracted from ECMWF analysis fields, for simMetOp data the "true" ECMWF analysis field profiles from the forward modeling were used as reference. This is the same setup as was used by Li et al. (2013).

3.1 Algorithm performance for individual profiles

Figure 6 illustrates the effects of statistical optimization on individual bending angle profiles by a few representative RO events. Observation uncertainty is smallest for the simMetOp event (top), largest for the CHAMP event (middle), and in between for the COSMIC event (bottom). At 60 km these observation uncertainties are roughly 0.4, 3, and 1.5 µrad for simMetOp, CHAMP, and COSMIC, respectively. Due to these differences in observation uncertainty, the altitude where the observation uncertainty equals the background uncertainty, which is more similar for all three events, is largest for simMetOp (> 60 km) and smallest for CHAMP (about 35 km).

Since bending angles increase roughly exponentially with decreasing altitude, as seen in the middle column of Fig. 6, differences among the various retrieved profiles seem to be small. The right panels, however, actually show the differences of optimized bending angle profiles relative to their reference. For the simMetOp event, bending angle differences are smallest over all altitudes from the dynamic algorithm, confirming the high utility of the algorithm, since here the "true" profile from forward simulations serves as reference. The bending angle differences of the b-dynamic algorithm are slightly larger than those from the dynamic algorithm, but the values are also small. The differences from the OPSv5.6 algorithm are largest, especially significantly more noisy.

For the CHAMP event the relative differences from the dynamic algorithm, the b-dynamic algorithm, and CDAAC are smaller than those from the OPSv5.6 algorithm below 50 km. Above 50 km, the relative differences from the dynamic algorithm increases

AMTD
8, 811–855, 2015

and are largest. For the COSMIC event, bending angles from the dynamic, b-dynamic and OPSv5.6 algorithms are rather similar below 50 km. Above 50 km, differences from the dynamic algorithm are tentatively largest. For this event, the differences of CDAAC are generally larger than the other three algorithms.

Inspecting further individual RO events (not shown) confirmed that the relative differences of simMetOp data from the dynamic algorithm are consistently smaller and smoother than those from the other approaches. This underlines the robust capability of the dynamic algorithm for improving the quality of the ionosphere-corrected bending angles. For CHAMP and COSMIC measurements, the relative differences from the dynamic algorithm are also generally smaller and smoother than those from other algorithms below 50 km. However, above 50 km, the differences from both the dynamic algorithm and from CDAAC are generally larger than those from the OPSv5.6 and b-dynamic approaches. This does not mean that bending angle profiles from the dynamic and CDAAC algorithms are not accurate at high altitude, however, it mainly depends on the determination of the weights of the background and observed bending angles in statistical optimization.

In the new dynamic algorithm, we currently use much larger relative background errors (e.g., around 40 %) at high altitudes (e.g., > 60 km) than OPSv5.6, which uses 15 % at all altitudes. At the same time the dynamically estimated observation uncertainties are usually smaller than those of OPSv5.6, which usually sets a large standard value (22 µrad) for events that are noisy at high altitudes. Therefore the new dynamic algorithm gives significantly more weight to the observed bending angles at high altitudes. In other words, if a user would want less observational weighting, this would need to be tuned by the bias coverage factor f_{bcvg} (cf. Eq. 3), which would accordingly modify the observation-to-background uncertainty ratio. For example, using a linear f_{bcvg} ranging from 1 at 80 km to 10 at 28 km, significantly changes the relative weighting compared to the baseline setting of $f_{\mathrm{bcvg}} = 5$ used for the algorithmic introduction by Li et al. (2013) and in this study.

AMTD
8, 811–855, 2015

Furthermore, similar as Li et al. (2013) did for the b-dynamic algorithm, we also inspected the effects of using two different correlation matrices, i.e., the estimated global-mean correlation matrices of our dynamic algorithm and the simple analytical correlation matrices constructed by exponential-falloff correlation functions with a correlation length of 10 km for background and 2 km for observation as used in the OPSv5.6 formulation. The dynamically estimated uncertainties were used for both cases, since we are interested only in the differences from the correlations in this particular inspection.

Figure 7 shows the comparison results for these two types of correlation matrices, again using three exemplary events from simMetOp, CHAMP, and COSMIC, showing absolute bending angles (left) and differences to reference (right). The simMetOp event highlights that bending angle differences from the full correlation case are much smoother and smaller than those from the exponential fall-off correlation. For the real CHAMP and COSMIC events, the magnitudes of the differences from the two cases are similar but also here it is clearly evident that use of the full correlation leads to smoother differences than use of exponential fall-off correlation. We conclude that the use of adequately realistic correlation matrices is preferable.

3.2 Statistical performance evaluation results

In this section the performance of the dynamic, b-dynamic, and OPSv5.6 statistical optimization algorithms are evaluated using simulated MetOp data from 15 January and 15 July 2008 and monthly CHAMP and COSMIC observations from January and July 2008. In addition, atmospheric profiles retrieved and provided by UCAR/CDAAC for the same time periods are used for comparison. The mean systematic differences between retrieved and reference profiles and the associated standard deviations are calculated and analyzed in bending angle, refractivity, and temperature profiles, similar to the statistical performance evaluation of the b-dynamic algorithm by Li et al. (2013), Sect. 3.3 therein.

In order to detect and exclude outlier profiles from the statistical profile ensembles, the quality of retrieved profiles is checked as follows. Bending angle profiles are

AMTD
8, 811–855, 2015

checked from 25 to 80 km and a profile is flagged bad if a bending angle exceeds a threshold at any impact altitude level, which was defined based on careful sensitivity tests as the maximum of either 40 µrad absolute or 25 % relative deviation from the co-located ECMWF short-range forecast bending angle. In practice, looking at it from top downwards, the transition from the absolute to the relative criterion occurs roughly around 35 km, where bending angle values start to exceed 160 µrad.

Refractivity and temperature profiles are checked in the same way as used for OPSv5.6/v5.4 (Schwaerz et al., 2013; Steiner et al., 2013; Pirscher, 2010), i.e., the deviation from co-located ECMWF analysis profiles at any altitude level must not exceed 10 % for refractivity between 5 and 35 km and 20 K for temperature within 8 and 25 km, respectively. These quality checks are performed to all profiles retrieved with the EGOPS software. For profiles provided by CDAAC, we check the CDAAC quality flag and use only profiles showing of good quality.

Figure 8 shows the systematic difference and standard deviations of optimized bending angle profiles of the global ensembles of simMetOp from 15 January and 15 July 2008, and of CHAMP and COSMIC events from January and July 2008. For simMetOp (top), it is clear to see that the performance of the dynamic algorithm outperforms the b-dynamic algorithm and the OPSv5.6 algorithm, exhibiting smallest systematic differences and associated standard deviations. Compared to the OPSv5.6 algorithm, the best improvement is found between 40 to 60 km. These results for the simulated events are very encouraging and confirm the fundamental capabilities of the dynamic algorithm.

Comparison of the CHAMP (middle) and COSMIC (bottom) results from the dynamic algorithm with the OPSv5.6 and CDAAC algorithms, shows that the bending angle standard deviation from the dynamic (and b-dynamic) algorithm is again generally smaller than that of the OPSv5.6 and CDAAC results. Below about 50 km this is due to the stronger weight that the dynamic algorithms give to the background for the bias coverage factor $f_{bcvg} = 5$ chosen here. If modifying f_{bcvg} to be somewhat larger over the stratosphere, i.e., penalizing the background uncertainty even more to increase the

Discussion Paper | Discussion Paper | Discussion Paper | Discussion Paper |

AMTD

8, 811–855, 2015

Dynamic statistical optimization of GNSS radio occultation bending angles

Y. Li et al.

weight on observations, the standard deviations from the dynamic algorithm increase. Our current illustrative choice with $f_{bcvg} = 5$ leads to what we consider the strongest reasonable standard deviation reduction in the stratosphere. Near 50 km for CHAMP, and more near 60 km for COSMIC, the standard deviations from the dynamic algorithm starts to exceed that from the OPSv5.6 algorithm. This is due to increased weight of noisy RO bending angles in the mesosphere compared to OPSv5.6 as discussed in Sect. 3.1 above. Standard deviations from both CDAAC data versions are larger than from the other approaches and particularly the new data version (shown for CHAMP) exhibits large increases of standard deviation already from about 35 km upwards.

Regarding systematic differences of CHAMP and COSMIC results from the reference (co-located ECMWF analysis profiles), these are rather similar for the dynamic, b-dynamic, and OPSv5.6 algorithms. The systematic differences from CDAAC algorithms are also similar, in particular below about 35 km, but are larger and of somewhat different character above about 40 km for July 2008 and in particular the new data version (shown for CHAMP) exhibits different (oscillatory) behavior both in January and July. These results indicated that the new dynamic algorithm is robust and competitive in providing optimized profiles with biases minimized in a best-possible manner, as should be expected from its realistic account for both observation and background uncertainties and error correlation structures.

Furthermore it is can be seen, in particular from the CHAMP results which represent the data of highest observational noise, that the improved treatment of the transition to pure-observed data around 30 km as discussed in Sect. 2.3 above has mitigated the sharpness of the change in standard deviation in case of still strong weight of background data near this height. For application in long-term climate processing an increased penalty to the background near 30 km (i.e., higher f_{bcvg}), then gradually decreasing over the stratosphere and mesosphere, may be considered a useful further improvement option.

In order to evaluate the performance of different statistical optimization algorithms in different latitude regions, the systematic differences and standard deviations of op-

AMTD
8, 811–855, 2015

timized bending angles were also calculated for five latitudinal bands in addition to the global case (90° S to 90° N), including tropics (TRO, 20° S to 20° N), Southern Hemisphere/Northern Hemisphere subtropics and mid-latitudes (SHSM/NHSM, 20 to 60° S/N), and Southern Hemisphere/Northern Hemisphere polar regions (SHP/NHP, 60 to 90° S/N). Figures 9, 10, and 11 show the statistical results for the global case (for context, same as in right column of Fig. 8) and for these five regions for simMetOp (Fig. 9), CHAMP (Fig. 10), and COSMIC (Fig. 11). The July 2008 results are shown which are found well representative; the latitude-resolved characteristics of the January 2008 results are similar.

Figure 9 shows that the performance of the dynamic, b-dynamic, and OPSv5.6 algorithms are rather similar globally and in the Northern Hemisphere (NHSM, NHP). In the Southern Hemisphere, and in particular in the SHP region (Antarctic winter in July), the conditions are evidently more challenging so that the OPSv5.6 algorithm accrues increased biases in the upper stratosphere above 50 km. The new dynamic algorithm underscores its good and reliable basic performance in all regions, both in terms of biases and standard deviations.

Figures 10 and 11 for the real bending angle data show that the performance of the dynamic, b-dynamic, OPSv5.6, and CDAAC algorithms in all latitude bands except SHP (Antarctic winter) is consistent and generally similar to the performance visible from the global ensemble, which we discussed along with Fig. 8 above. In SHP, both systematic differences and standard deviations are markedly larger. In particular the CDAAC results, and most so the new CDAAC data version, exhibit relatively large systematic differences at these heights (up to around 5 %) and also standard deviations closely reaching to or exceeding 10 % already at altitudes near 50 km. Error characteristics for January (not shown) in the NHP region (Arctic winter) generally mirror the SHP July (Antarctic winter) error characteristics.

We consider the new dynamic algorithm in this context to confirm its robust performance also for real data in all regions, although the lack of a “true” reference in these cases does not allow for strong conclusions. In evaluating future long-term processing

AMTD
8, 811–855, 2015

application of the algorithm, we will also include more strict validation against independent co-located data of high quality over the stratosphere and mesosphere from other sources such as the Envisat/MIPAS and Timed/SABER satellite instruments (Remsberg et al., 2008; Garcia-Comas et al., 2012).

Figures 12 and 13 show the global statistics results for refractivity (Fig. 12) and temperature (Fig. 13), respectively, for simMetOp (top), CHAMP (middle), and COSMIC (bottom). These refractivity and temperature results reflect the results for the bending angles in a filtered manner, after having passed through the Abelian integration (refractivity) and in addition the hydrostatic integration (temperature), which lead to smoothing and downward propagation of biases and to reduction of standard deviations (e.g., Gobiet and Kirchengast, 2004; Steiner and Kirchengast, 2005). Due to this downward propagation, the differences from the various algorithms become smaller and results are closely similar below about 40 km and in most cases even above. The most notable differences from the consistent behavior of the different algorithms are those of the CDAAC versions above about 50 km, which exhibit the largest systematic differences and standard deviations, and the additional deviations of the new CDAAC version (shown for CHAMP) already from about 35 km upwards.

Again we consider the performance seen in this context for the new dynamic algorithm robust and encouraging for larger-scale application, which may also include further fine-tuning of parameters like f_{bcvg} and of averaging domains for constructing the dynamic uncertainty and correlation information.

Figure 14 extends the view of Fig. 7 on the sensitivity to the choice of correlation modeling to a statistical view. It depicts the results of global statistics for simMetop (top) and COSMIC (bottom), for bending angle (left), refractivity (middle), and temperature (right), from either operating the full dynamic algorithm or from using simplified correlation modeling with the exponential fall-off approximation. The simMetOp results show, in line with the results of Fig. 7, that the use of the realistically modeled full correlations is a superior choice, though the reduction of systematic difference relative to the “true” reference is small (after the Abel resp. hydrostatic integrations) in refractivity

AMTD
8, 811–855, 2015

and temperature. The COSMIC results indicate that the choice of correlation modeling strongly impacts the standard deviation and to a more limited degree also the systematic differences. While this behavior does, on its own, not imply a preference it is very clear that the choice of the realistic full correlation modeling will be the physically more sound and more adequate approach also for real data.

4 Summary and conclusions

This study presented a new dynamic statistical optimization algorithm to initialize RO ionosphere-corrected bending angle at high altitudes for optimal climate monitoring throughout the stratosphere. This dynamic algorithm uses multiple days of ECMWF analysis, ECMWF short-range (24 h) forecast, and RO observation data to realistically estimate background and observation error covariance matrices. Both the background and observation error covariance matrices are constructed with geographically-varying uncertainty estimation and with a global-mean correlation matrix estimated on a daily updated basis. The b-dynamic algorithm recently introduced by Li et al. (2013) was used as starting point and provided for the estimation of background error covariance matrix and the bias-correction of background bending angles.

The main advancements of the new dynamic algorithm compared to this previous algorithm are: (1) adds a dynamically estimated observation error covariance matrix with altitude-dependent observation uncertainty and a realistically calculated global-mean correlation matrix; (2) updates the algorithm of the calculation of basic statistical mean variables by using ECMWF and RO data from a longer time window and larger geographical regions for more accurate and reliable estimation; (3) eliminates weaknesses that existed near the lower boundary of statistical optimization (30 km) by improving the uncertainty formulation and transition to pure-observed data across this boundary.

We illustrated and discussed key variables of the dynamic background and observation error covariance matrices, including systematic and random uncertainties and correlation functions, in order to provide insight and show the realistic character of

AMTD

8, 811–855, 2015

Dynamic statistical optimization of GNSS radio occultation bending angles

Y. Li et al.

their behavior. Both the random and systematic background uncertainties appear to be largest in the polar regions of the winter hemisphere at mesospheric altitudes. The observation uncertainties capture variations with altitude, especially in the mesosphere, and can well represent the error characteristics of RO events, from high-quality simulated data to comparatively noisy CHAMP data. The observation error correlation functions show similar shape as for background data, but with less functional smoothness and with much smaller correlation lengths of about 0.8 km (while background error correlation lengths range from about 1 near 20 km to about 6 near 80 km). All uncertainty and correlation estimates were found to exhibit little sub-monthly variations during the test months January and July 2008. In case of anomalous sub-monthly conditions (e.g., sudden stratospheric warming) that will occasionally happen during long-term processing periods, we expect more variation, however.

The new dynamic algorithm was evaluated mainly against the one currently used in the OPSv5.6 system, using simulated MetOp data on single days (15 January and 15 July 2008) and real observed CHAMP and COSMIC data from two full months (January and July 2008). The following was found for the new dynamic algorithm, in particular compared to OPSv5.6: (1) it can reduce systematic errors (biases) and standard deviations of optimized bending angles, as proven by simMetOp data including also “true” reference profiles from end-to-end simulations, and subsequently also benefits the error characteristics of retrieved refractivity and temperature profiles; (2) it can reduce the random errors of optimized bending angles in the stratosphere for real data, as evaluated for CHAMP and COSMIC data, still at the same time leaving less or about equal residual systematic errors (biases) in the bending angles; (3) it can better account for the observational noise in the mesosphere, leading to larger standard deviations than OPSv5.6 there from higher weight on the observations in the optimized profiles, but without applying any artificial observation uncertainty values in case of high noise.

Beyond the evaluation of the new dynamic algorithm against OPSv5.6, atmospheric profiles from UCAR/CDAAC were also inter-compared, including use of very recently released CHAMP data from the newest (2014) CDAAC data version. It was found that

AMTD
8, 811–855, 2015

CDAAC bending angles generally exhibit markedly higher standard deviations above about 35 km and that in particular the new data version shows comparatively large systematic differences and standard deviations. The reasons for this new-version behavior deserve further study, including based on COSMIC data in addition to CHAMP data.

Overall, compared to previous simplified approaches of statistical optimization, the dynamic algorithm presented here, which realistically estimate both background and observation error covariance matrices, contains high capabilities for future large-scale implementation. The evaluation of the algorithm provided clear evidence that it can deliver reliable and accurate atmospheric profiles for atmosphere and climate applications. The results therefore indicate high suitability for employing the new dynamic approach in the processing of long-term RO data into a climate record, leading to well characterized and high-quality atmospheric profiles over the entire stratosphere.

Acknowledgements. We thank M. Bonavita and S. B. Healy (ECMWF Reading, UK) for valuable advice related to ECMWF's analysis and forecast and associated error characteristics and are thankful for fruitful discussions within the IGMAS group at the IGG (Wuhan, China) and to Suqin Wu at RMIT. We also thank UCAR/CDAAC for access to their RO data as well as ECWMF for access to their analysis and forecast data. Furthermore, we acknowledge the funding support by China Natural Science Funds (No. 41231064, No. 41021003), National 973 (No. 2012CB825604), China Scholarship Council, and CAS/SAFEA International Partnership Program for Creative Research Teams (KZZD-EW-TZ-05) at the IGG side, the funding support by the Australian Space Research Program (ASRP2), the Australian Antarctic Science (AAS) Grant project (AAS 4159) and the Australian Natural Disaster Resilience Grant Scheme (NDRG) of Victoria at the RMIT side, and the funding support by the European Space Agency (ESA) project OPSGRAS, the Austrian Research Promotion Agency (FFG) project OPSCLIMTRACE, and the Austrian National Science Fund (FWF) project DYNOCC (T620-N29) at the WEGC side.

References

Anthes, R. A.: Exploring Earth's atmosphere with radio occultation: contributions to weather, climate and space weather, Atmos. Meas. Tech., 4, 1077–1103, doi:10.5194/amt-4-1077-2011, 2011.

Bassiri, S. and Hajj, G. A.: Higher-order ionospheric effects on the GPS observables and means of modeling them, Manuscr. Geod., 18, 280–289, 1993.

Bonavita, M., Raynaud, L., and Isaksen, L.: Estimating background error variances with the ECMWF Ensemble of Data Assimilations system: some effects of ensemble size and day-to-day variability, Q. J. Roy. Meteor. Soc., 137, 423–434, doi:10.1002/qj.756, 2011.

Carter, B. A., Zhang, K., Norman, R., Kumar, V. V., and Kumar, S.: On the occurrence of equatorial F-region irregularities during solar minimum using radio occultation measurements, J. Geophys. Res. Space Phys., 118, 892–904, doi:10.1002/jgra.50089, 2013.

Cucurull, L. and Derber, J. C.: Operational implementation of COSMIC observations into NCEP's global data assimilation system, Wea. Forecasting., 23, 702–711, doi:10.1175/2008WAF2007070.1, 2008.

Danzer, J., Scherllin-Pirscher, B., and Foelsche, U.: Systematic residual ionospheric errors in radio occultation data and a potential way to minimize them, Atmos. Meas. Tech., 6, 2169–2179, doi:10.5194/amt-6-2169-2013, 2013.

Fritzer, J., Kirchengast, G., and Pock, M.: End-to-End Generic Occultation Performance Simulation and Processing System version 5.6 (EGOPS 5.6) Software User Manual, Tech. Rep. ESA/ESTEC-1/2013, Wegener Center, University of Graz, Graz, Austria, 2013.

Gaspari, G. and Cohn, S. E.: Construction of correlation functions in two and three dimensions, Q. J. Roy. Meteor. Soc., 125, 723–757, 1999.

García-Comas, M., Funke, B., López-Puertas, M., Bermejo-Pantaleón, D., Glatthor, N., von Clarmann, T., Stiller, G., Grabowski, U., Boone, C. D., French, W. J. R., Leblanc, T., López-González, M. J., and Schwartz, M. J.: On the quality of MIPAS kinetic temperature in the middle atmosphere, Atmos. Chem. Phys., 12, 6009–6039, doi:10.5194/acp-12-6009-2012, 2012.

Gobiet, A. and Kirchengast, G.: Advancements of Global Navigation Satellite System radio occultation retrieval in the upper stratosphere for optimal climate monitoring utility, J. Geophys. Res., 109, D24110, doi:10.1029/2004JD005117, 2004.

Gobiet, A., Kirchengast, G., Manney, G. L., Borsche, M., Retscher, C., and Stiller, G.: Retrieval of temperature profiles from CHAMP for climate monitoring: intercomparison with Envisat MIPAS and GOMOS and different atmospheric analyses, Atmos. Chem. Phys., 7, 3519–3536, doi:10.5194/acp-7-3519-2007, 2007.

Gorbunov, M. E.: Ionospheric correction and statistical optimization of radio occultation data, Radio Sci., 37, 1084, doi:10.1029/2000RS002370, 2002.

Gorbunov, M. E., Gurvich, A. S., and Bengtsson, L.: Advanced algorithms of inversion of GPS/MET satellite data and their application to reconstruction of temperature and humidity, Report No 211, Max-Planck-Institute for Meteorology, Hamburg, 1996.

Gorbunov, M. E., Lauritsen, K. B., Rhodin, A., Tomassini, M., and Kornblueh, L.: Analysis of the CHAMP experimental data on radio-occultation sounding of the Earth's atmosphere, Izv. Atmos. Ocean. Phys., 41, 726–740, 2005.

Gorbunov, M. E., Lauritsen, K. B., Rhodin, A., Tomassini, M., and Kornblueh, L.: Radio holographic filtering, error estimation, and quality control of radio occultation data, J. Geophys. Res., 111, D10105, doi:10.1029/2005JD006427, 2006.

Hajj, G. A., Kursinski, E. R., Romans, L. J., Bertiger, W. I., and Leroy, S. S.: A technical description of atmospheric sounding by GPS occultation, J. Atmos. Sol. Terr. Phys., 64, 451–469, doi:10.1016/S1364-6826(01)00114-6, 2002.

Healy, S. B.: Smoothing radio occultation bending angles above 40 km, Ann. Geophys., 19, 459–468, doi:10.5194/angeo-19-459-2001, 2001.

Healy, S. B. and Eyre, J. R.: Retrieving temperature, water vapour and surface pressure information from refractive-index profiles derived by radio occultation: a simulation study, Q. J. Roy. Meteor. Soc., 126, 1661–1683, doi:10.1002/qj.49712656606, 2000.

Ho, S.-P., Hunt, D., Steiner, A. K., Mannucci, A. J., Kirchengast, G., Gleisner, H., Heise, S., von Engeln, A., Marquardt, C., Sokolovskiy, S., Schreiner, W., Scherllin-Pirscher, B., Ao, C., Wickert, J., Syndergaard, S., Lauritsen, K. B., Leroy, S., Kursinski, E. R., Kuo, Y.-H., Foelsche, U., Schmidt, T., and Gorbunov, M.: Reproducibility of GPS radio occultation data for climate monitoring: profile-to-profile inter-comparison of CHAMP climate records 2002 to 2008 from six data centers, J. Geophys. Res., 117, D18111, doi:10.1029/2012JD017665, 2012.

Hocke, K.: Inversion of GPS meteorology data, Ann. Geophys., 15, 443–450, doi:10.1007/s00585-997-0443-1, 1997.

Isaksen, L., Haseler, J., Buizza, R., and Leutbecher, M.: The new Ensemble of Data Assimilations, ECMWF Newsl., 123, 17–21, 2010.

AMTD
8, 811–855, 2015

Kirchengast, G.: Occultations for probing atmosphere and climate: setting the scene, in: Occultations for Probing Atmosphere and Climate, edited by: Kirchengast, G., Foelsche, U., and Steiner, A. K., 1–8, Springer, Berlin-Heidelberg, 2004.

Klingler, R.: Observing sudden stratospheric warmings with radio occultation data, with focus on the event 2009 (MSc thesis), Wegener Center and Institute of Physics, University of Graz, Graz, Austria, 2014.

Kursinski, E. R., Hajj, G. A., Schofield, J. T., Linfield, R. P., and Hardy, K. R.: Observing Earth's atmosphere with radio occultation measurements using the Global Positioning System, J. Geophys. Res., 102, 23429–23465, doi:10.1029/97JD01569, 1997.

Leitinger, R., Titheridge, J. E., Kirchengast, G., and Rothleitner, W.: A 'simple' global empirical model for the F layer of the ionosphere, Kleinheubacher Ber., 39, 697–704, 1996 (in German; English version available from co-author Kirchengast).

Le Marshall, J., Xiao, Y., Norman, R., Zhang, K., Rea, A., Cucurull, L., Seecamp, R., Steinle, P., Puri, K., and Le, T.: The beneficial impact of radio occultation observations on Australian region forecasts, Aust. Meteorol. Oceanogr. J., 60, 121–125, 2010.

Li, Y.: A new dynamic approach for the statistical optimization of GNSS radio occultation bending angles (PhD thesis), RMIT University, Melbourne, Australia, 2013.

Li, Y., Kirchengast, G., Scherllin-Pirscher, B., Wu, S., Schwaerz, M., Fritzer, J., Zhang, S., Carter, B. A., and Zhang, K.: A new dynamic approach for statistical optimization of GNSS radio occultation bending angles for optimal climate monitoring utility, J. Geophys. Res., 118, 13022–13040, doi:10.1002/2013JD020763, 2013.

Liu, C. L., Kirchengast, G., Zhang, K. F., Norman, R., Li, Y., Zhang, S. C., Carter, B., Fritzer, J., Schwaerz, M., Choy, S. L., Wu, S. Q., and Tan, Z. X.: Characterisation of residual ionospheric errors in bending angles using GNSS RO end-to-end simulations, Adv. Space Res., 52, 821–836, doi:10.1016/j.asr.2013.05.021, 2013.

Lohmann, M. S.: Application of dynamical error estimation for statistical optimization of radio occultation bending angles, Radio Sci., 40, RS3011, doi:10.1029/2004RS003117, 2005.

Pirscher, B.: Multi-satellite climatologies of fundamental atmospheric variables from radio occultation and their validation (Ph. D. thesis), Wegener Center Verlag Graz, Sci. Rep. 33–2010, 2010.

Remsberg, E. E., Marshall, B. T., Garcia-Comas, M., Krueger, D., Lingenfelser, G. S., Martin-Torres, J., Mlynczak, M. G., Russell, J. M., Smith, A. K., Zhao, Y., Brown, C., Gordley, L. L., Lopez-Gonzalez, M. J., Lopez-Puertas, M., She, C.-Y., Taylor, M. J., and Thomp-

AMTD
8, 811–855, 2015

Dynamic statistical optimization of GNSS radio occultation bending angles

Y. Li et al.

son, R. E.: Assessment of the quality of the Version 1.07 temperature-versus-pressure profiles of the middle atmosphere from TIMED/SABER, J. Geophys. Res. Atmos., 113, D17101, doi:10.1029/2008JD010013, 2008.

Rieder, M. J. and Kirchengast, G.: Error analysis and characterization of atmospheric profiles retrieved from GNSS occultation data, J. Geophys. Res., 106, 31755–31770, doi:10.1029/2000JD000052, 2001.

Rodgers, C. D.: Retrieval of atmospheric temperature and composition from remote measurements of thermal radiation, Rev. Geophys., 14, 609–624, doi:10.1029/RG014i004p00609, 1976.

Rodgers, C. D.: Inverse Methods for Atmospheric Sounding: theory and Practice, World Scientific Publ., Singapore, doi:10.1142/9789812813718, 2000.

Schwaerz, M., Scherllin-Pirscher, B., Kirchengast, G., Schwarz, J., Ladstaedter, F., Fritzer, J., and Ramsauer, J.: MMValRO-CCN3 – Multi-Mission Validation by Satellite Radio Occultation (Final Report), Tech. Rep. ESA/ESRIN-1/2013, Wegener Center, University of Graz, Graz, Austria, 2013.

Sokolovskiy, S. and Hunt, D.: Statistical optimization approach for GPS/MET data inversion, paper presented at the URSI GPS/MET workshop, Union Radio Sci. Int., Tucson, Ariz., 1996.

Steiner, A. K. and Kirchengast, G.: Error analysis for GNSS radio occultation data based on ensembles of profiles from end-to-end simulations, J. Geophys. Res., 110, D15307, doi:10.1029/2004JD005251, 2005.

Steiner, A. K., Lackner, B. C., Ladstädter, F., Scherllin-Pirscher, B., Foelsche, U., and Kirchengast, G.: GPS radio occultation for climate monitoring and change detection, Radio Sci., 46, RS0D24, doi:10.1029/2010RS004614, 2011.

Steiner, A. K., Hunt, D., Ho, S.-P., Kirchengast, G., Mannucci, A. J., Scherllin-Pirscher, B., Gleisner, H., von Engeln, A., Schmidt, T., Ao, C., Leroy, S. S., Kursinski, E. R., Foelsche, U., Gorbunov, M., Heise, S., Kuo, Y.-H., Lauritsen, K. B., Marquardt, C., Rocken, C., Schreiner, W., Sokolovskiy, S., Syndergaard, S., and Wickert, J.: Quantification of structural uncertainty in climate data records from GPS radio occultation, Atmos. Chem. Phys., 13, 1469–1484, doi:10.5194/acp-13-1469-2013, 2013.

Turchin, V. F. and Nozik, V. Z.: Statistical regularization of the solution of incorrectly posed problems, Izvestiya, Atmospheric and Oceanic Phys., Engl. Transl., 5, 14–18, 1969.

AMTD

8, 811–855, 2015

Yu, K., Rizos, C., Burrage, D., Dempster, A., Zhang, K., and Markgraf, M.: An Overview of GNSS Remote Sensing, EURASIP J. Adv. Sig. Pr., 134, doi:10.1186/1687-6180-2014-134, 2014.

AMTD

8, 811–855, 2015

Dynamic statistical optimization of GNSS radio occultation bending angles

Y. Li et al.

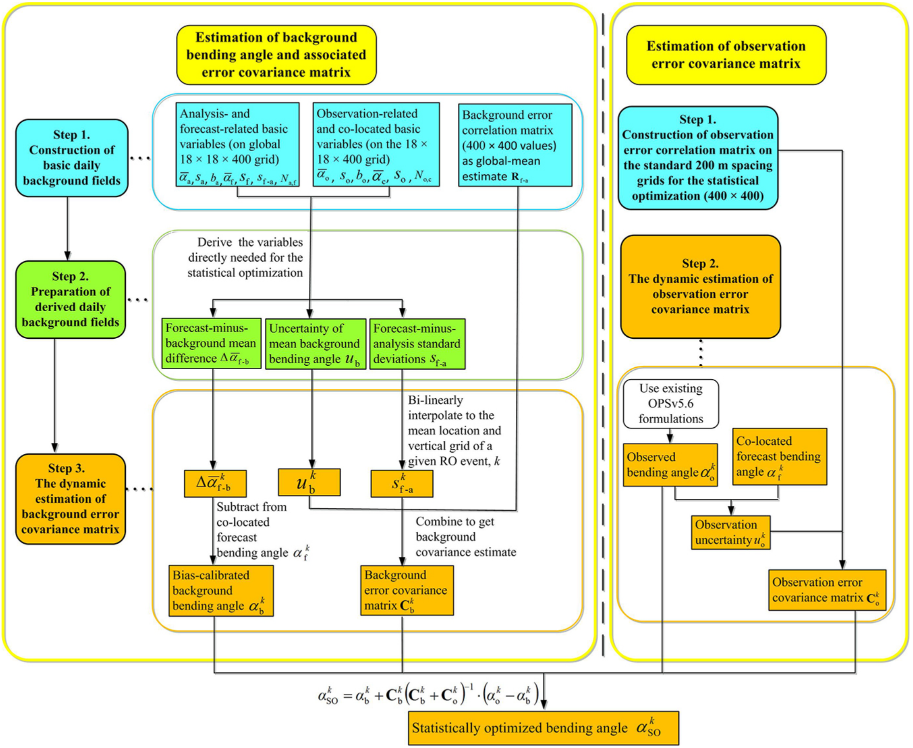

Figure 1. Schematic illustration of the algorithmic steps of the dynamic statistical optimization approach; for description see Sects. 2.1 and 2.2.

AMTD
8, 811–855, 2015

Dynamic statistical optimization of GNSS radio occultation bending angles

Y. Li et al.

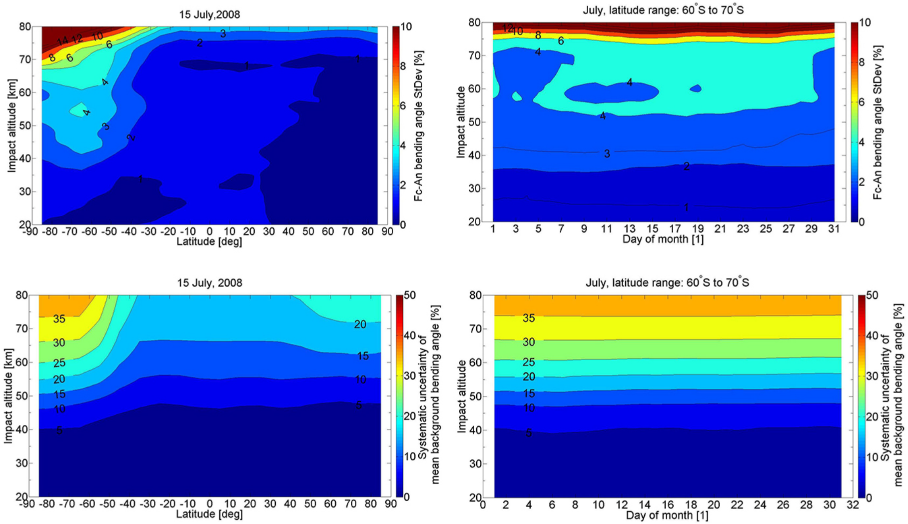

Figure 2. Variability of relative standard deviations of forecast-minus-analysis bending angle differences (upper two panels) and of the systematic uncertainty of mean background bending angles (bottom two panels) as function of latitude (left) and of day of month (right), respectively.

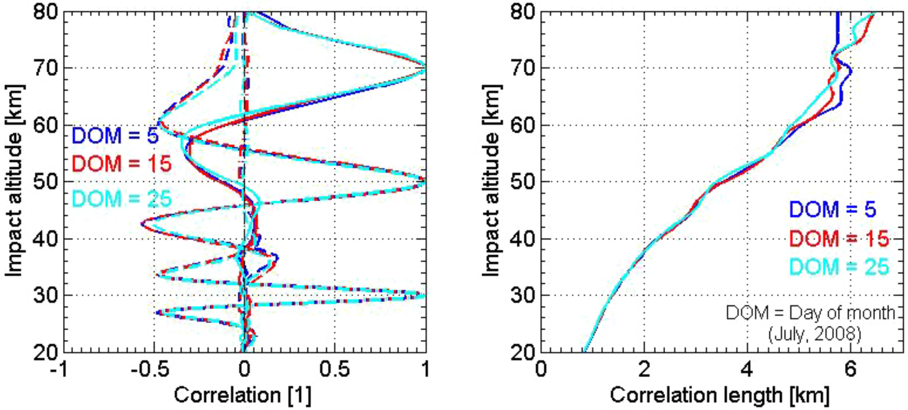

Figure 3. Global mean error correlation functions from the background error covariance matrix (left), for the 5, 15, and 25 July 2008 at three representative impact altitude levels (30, 50, and 70 km), and estimated correlation lengths of the correlation functions (right) at all impact altitude levels from 20 to 80 km for the same three days.

AMTD
8, 811–855, 2015

Dynamic statistical optimization of GNSS radio occultation bending angles

Y. Li et al.

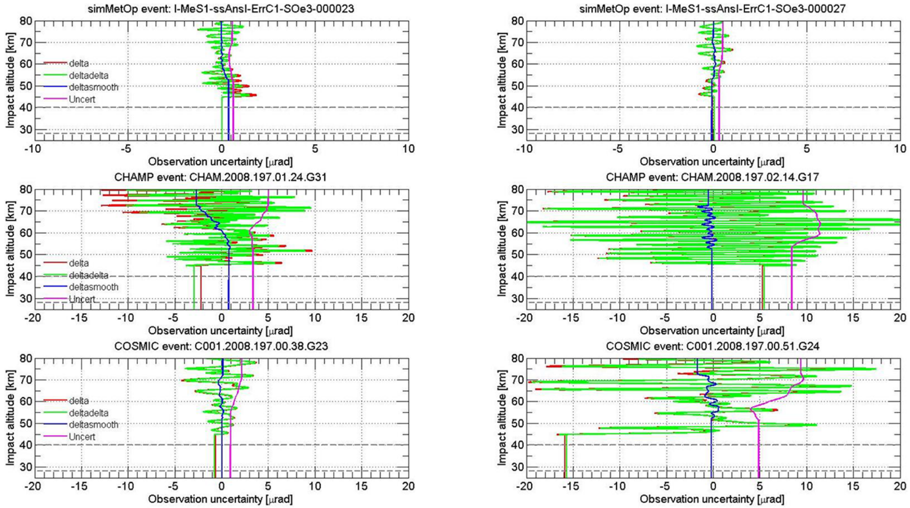

Figure 4. Observation uncertainty and key intermediate variables for six representative RO events, two simMetOp events (top), two CHAMP events (middle), and two COSMIC events (bottom) from 15 July 2008. "delta" is the difference profile of the RO ionosphere-corrected bending angle to the co-located ECMWF analysis profile used as reference, "deltadelta" is the delta-difference profile after subtracting a smoothed profile "deltasmooth" from the difference profile "delta", and "Uncert" is the resulting observation uncertainty estimate; for detailed description see Sect. 2.2.

AMTD

8, 811–855, 2015

Dynamic statistical optimization of GNSS radio occultation bending angles

Y. Li et al.

Title Page
Abstract | Introduction
Conclusions | References
Tables | Figures
◀| |▶
◀ ▶
Back | Close
Full Screen / Esc
Printer-friendly Version
Interactive Discussion

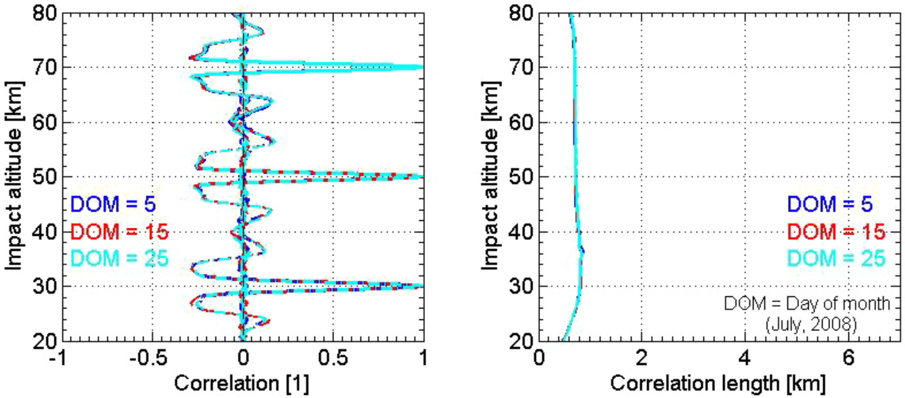

Figure 5. Global mean error correlation functions from the observation error covariance matrix (left), for the 5, 15, and 25 July 2008 at three representative impact altitude levels (30, 50, and 70 km), and estimated correlation lengths of the correlation functions (right) at all impact altitude levels from 20 to 80 km for the same three days. For ease of inter-comparison the layout is the same as in Fig. 3.

AMTD
8, 811–855, 2015

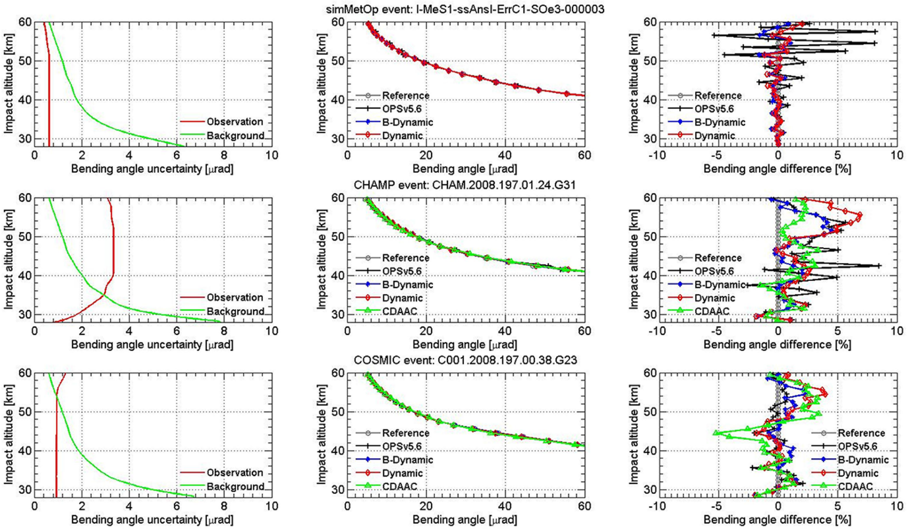

Figure 6. Background and observation bending angle uncertainty profiles (left), statistically optimized bending angle profiles from the OPSv5.6, b-dynamic, dynamic, and CDAAC algorithms together with their reference profile (middle), and difference of the optimized profiles to the reference profile (right). Three example events from 15 July 2008 are illustrated, from simMetOp (top), CHAMP (middle), and COSMIC (bottom), respectively.

AMTD
8, 811–855, 2015

Dynamic statistical optimization of GNSS radio occultation bending angles

Y. Li et al.

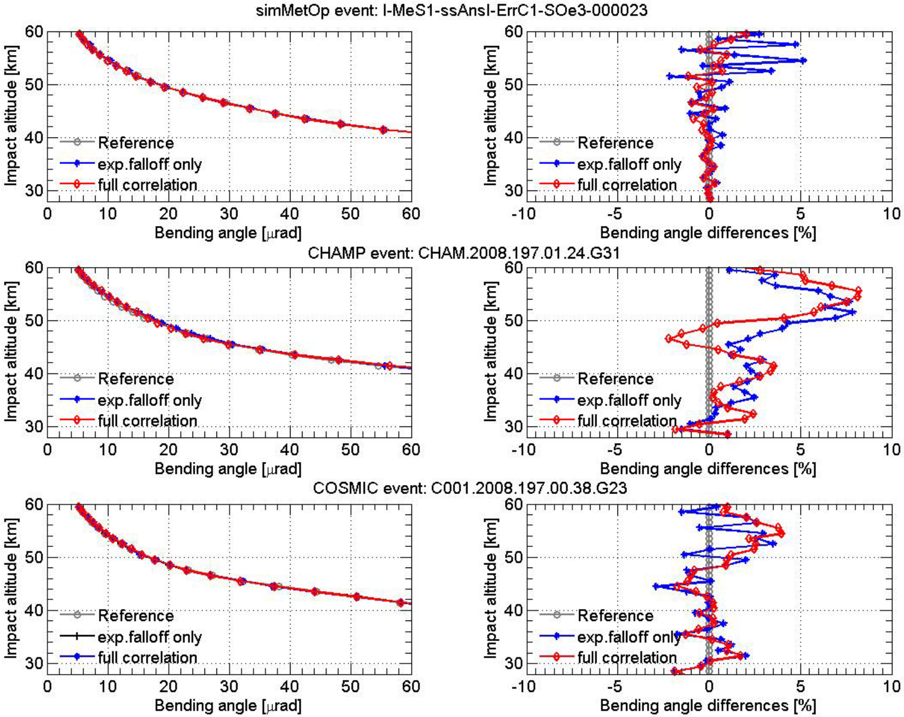

Figure 7. Statistically optimized bending angle profiles together with their reference profile (left) and their difference to the reference profile (right), of three example events from simMetOp (top), CHAMP (middle), and COSMIC (bottom) from 15 July 2008, using either the realistic global-mean correlation matrix of the new dynamic method ("full correlation") or simple exponential fall-off correlation as existing in OPSv5.6 ("exp.falloff only").

AMTD
8, 811–855, 2015

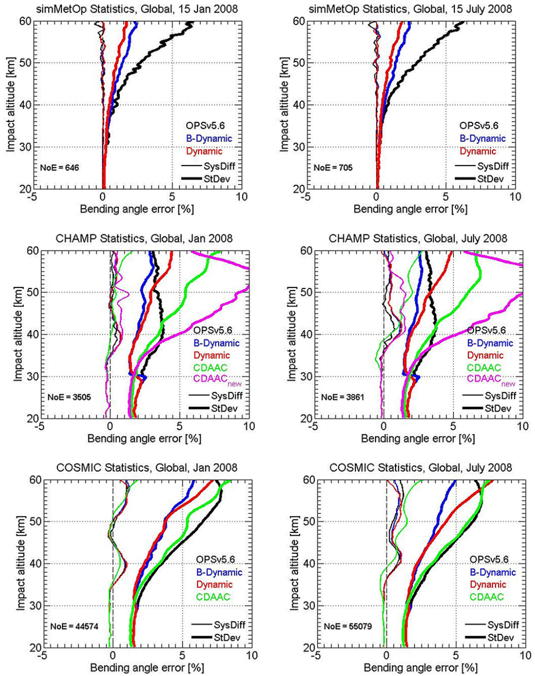

Figure 8. Systematic differences (SysDiff, light lines) and standard deviations (StDev, heavy lines) of statistically optimized bending angles, relative to "perfect" simulated bending angles or co-located ECMWF analysis bending angles used as references, of the global ensemble of simMetOp events on 15 January and 15 July 2008 (upper two panels), and of CHAMP and COSMIC events from the complete months of January and July 2008 (middle and bottom panels, respectively). Statistics of the OPSv5.6 (black), b-dynamic (blue), dynamic (red), CDAAC (version 2009.2650 for CHAMP and version 2010.2640 for COSMIC, green), and $\text{CDAAC}_{\text{new}}$ (version 2014.0140 for CHAMP, magenta) statistical optimization methods are shown. The number of events (NoE) used in the ensemble of each statistical calculation is also indicated in each panel.

AMTD
8, 811–855, 2015

Dynamic statistical optimization of GNSS radio occultation bending angles

Y. Li et al.

AMTD
8, 811–855, 2015

Dynamic statistical optimization of GNSS radio occultation bending angles

Y. Li et al.

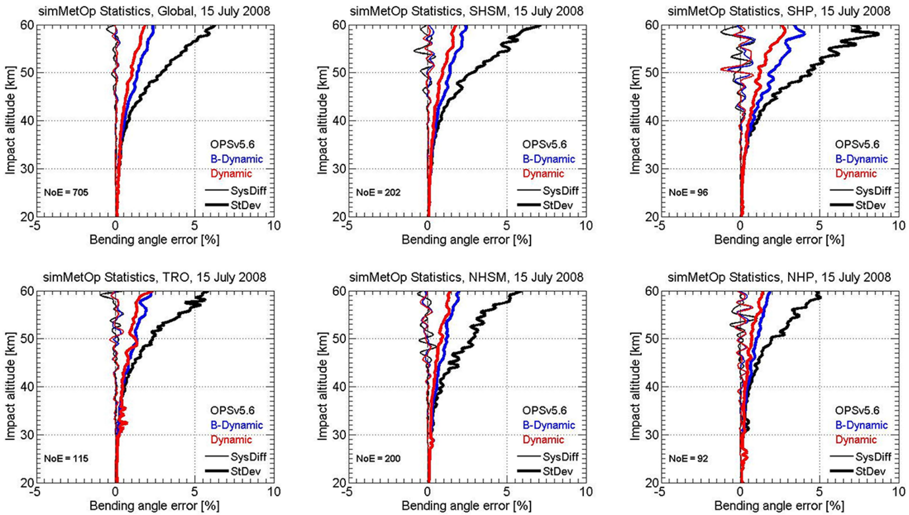

Figure 9. Systematic differences (SysDiff, light lines) and standard deviations (StDev, heavy lines) of statistically optimized bending angles, relative to "perfect" simulated bending angles used as reference, of simMetOp events on 15 July 2008. Statistics for the OPSv5.6 (black), b-dynamic (blue), and dynamic (red) statistical optimization algorithms are shown for six different regions: global (90° S to 90° N), TRO (tropics, 20 to 20° N), SHSM (Southern Hemisphere subtropics and mid-latitudes, 20 to 60° S), NHSM (Northern Hemisphere subtropics and mid-latitudes, 20 to 60° N), SHP (Southern Hemisphere polar region, 60 to 90° S), and NHP (Northern Hemisphere polar region, 60 to 90° N). The number of events (NoE) used in the ensemble of each region is also indicated in the panels.

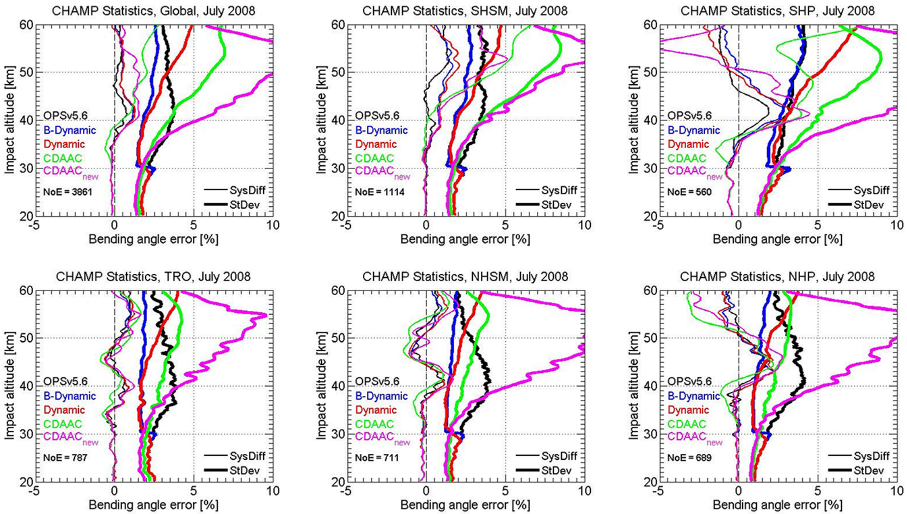

Figure 10. Systematic differences (SysDiff, light lines) and standard deviations (StDev, heavy lines) of statistically optimized bending angles, relative to co-located ECMWF analysis bending angles used as reference, of CHAMP events from July 2008. Statistics for the OPSv5.6 (black), b-dynamic (blue), dynamic (red), CDAAC (version 2009.2650, green), and $\text{CDAAC}_{\text{new}}$ (version 2014.014, magenta) statistical optimization algorithms are shown for the same six regions as in Fig. 9. The figure layout is the same as for Fig. 9.

AMTD
8, 811–855, 2015

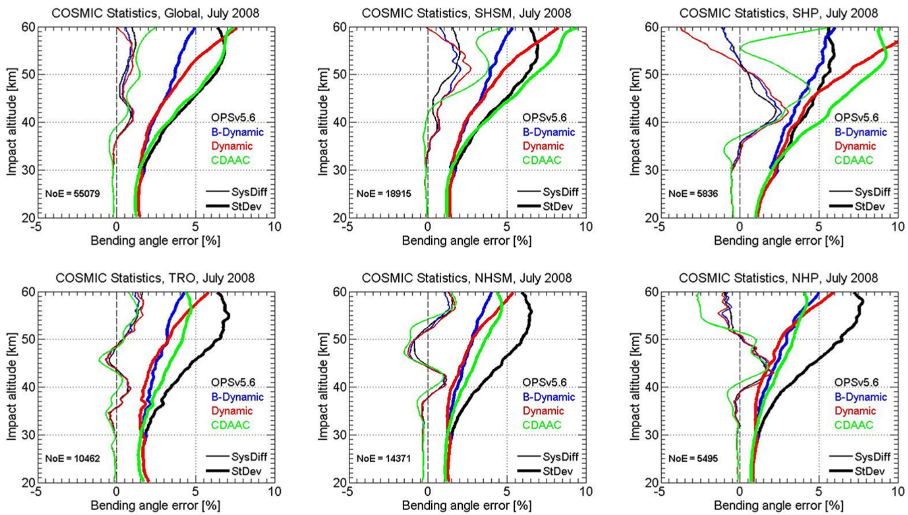

Figure 11. Systematic differences (SysDiff, light lines) and standard deviations (StDev, heavy lines) of statistically optimized bending angles, relative to co-located ECMWF analysis bending angles used as reference, of COSMIC events from July 2008. Statistics for the OPSv5.6 (black), b-dynamic (blue), dynamic (red), and CDAAC (version 2010.2640, green) statistical optimization algorithms are shown for the same six regions as in Fig. 9. The figure layout is the same as for Figs. 9 and 10.

AMTD
8, 811–855, 2015

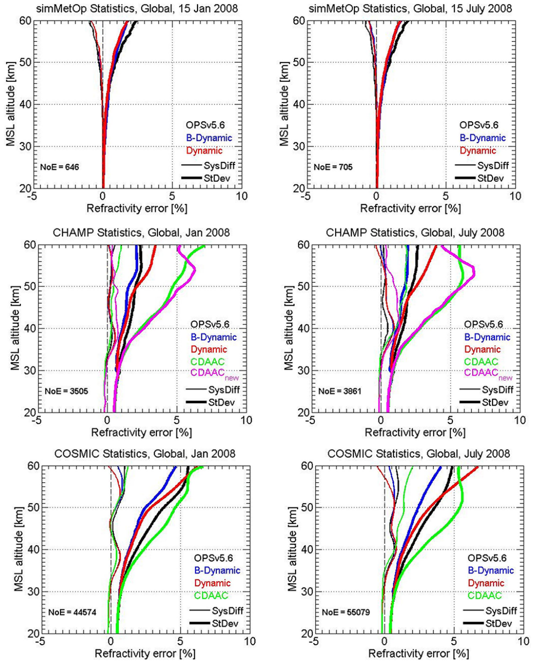

Figure 12. Systematic differences (SysDiff, light lines) and standard deviations (StDev, heavy lines) of retrieved refractivity profiles, relative to "perfect" simulated bending angles or co-located ECMWF analysis refractivity used as reference, for the global ensemble of simMetOp events on 15 January and 15 July 2008 (top panels) and of CHAMP events (middle panels) and COSMIC events (bottom panels) from the complete months of January and July 2008. Statistics of the OPSv5.6 (black), b-dynamic (blue), dynamic (red), CDAAC (version 2009.2650 for CHAMP and version 2010.2640 for COSMIC, green), and CDAACnew (version 2014.0140 for CHAMP, magenta) statistical optimization methods are shown. The figure layout is the same as for Fig. 8.

AMTD
8, 811–855, 2015

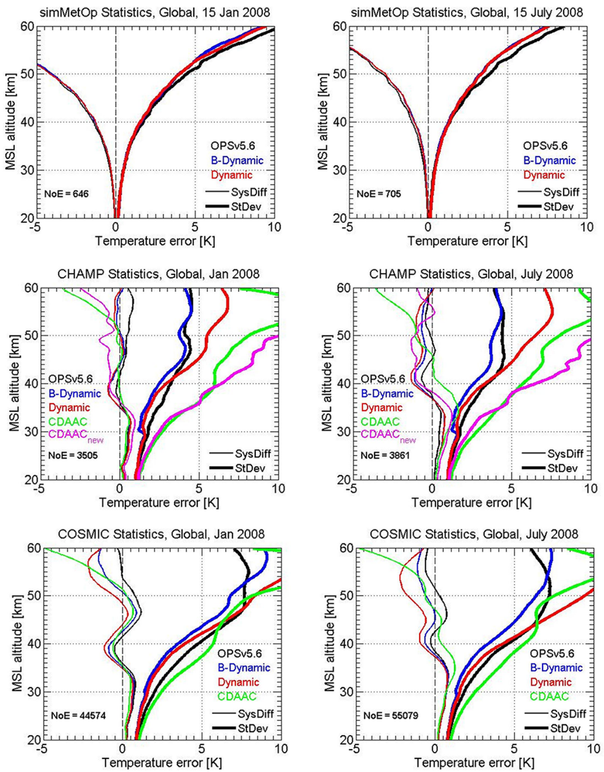

Figure 13. Systematic differences (SysDiff, light lines) and standard deviations (StDev, heavy lines) of retrieved temperature profiles, relative to "perfect" simulated bending angles or co-located ECMWF analysis temperature used as reference, for the global ensemble of simMetOp events on 15 January and 15 July 2008 (top panels) and of CHAMP events (middle panels) and COSMIC events (bottom panels) from the full months of January and July 2008. The figure layout and data sources shown are the same as in Figs. 8 and 12.

AMTD
8, 811–855, 2015

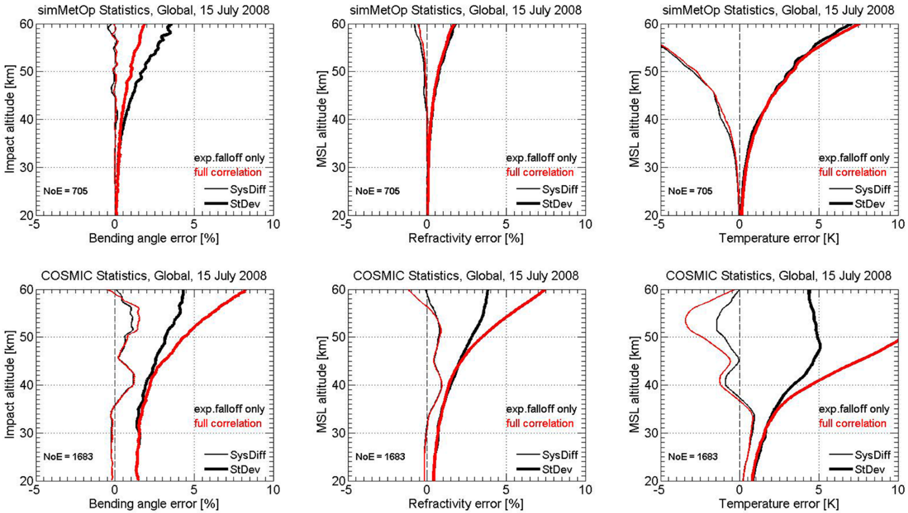

Figure 14. (Left) Bending angle, (middle) refractivity, and (right) temperature systematic differences (SysDiff, light lines) and standard deviations (StDev, heavy lines), relative to their "perfect simulated" or co-located ECMWF analysis data used as reference, of the global ensemble of (top) simMetOp and (bottom) COSMIC events from 15 July 2008, using either the realistic global-mean correlation matrix of the new dynamic method ("full correlation") or simple exponential fall-off correlation as in the existing OPSv5.6 ("exp.falloff only"). The number of events (NoE) in each statistical ensemble is also indicated in the panels.

AMTD
8, 811–855, 2015